# High-fidelity simulation of boundary layer flow over waves

### By J. Wu† AND H. Hwang

We extend the high-fidelity, two-phase, fully coupled simulations of wind-wave interaction from Wu *et al.* (2022), with a focus on the dynamics of the wave-modulated boundary layer. In addition to the previous pressure-gradient-based forcing, we implement a new forcing method inspired by the near-wall-patch configuration to impose a constant mean momentum flux through the upper simulation boundary. We analyze various statistics, including triple decomposition, vertical profiles of turbulent and wave-induced stresses, horizontal wavenumber spectra across different cross sections, and mean velocity profiles alongside the corresponding roughness parameter. The sensitivity of these statistics to forcing methods is reported. Finally, we discuss the implication of the roughness length parameter and potential applications of our high-fidelity simulations for improving wind-wave models.

---

## 1. Introduction

Surface waves are ubiquitous over the ocean. They respond to wind forcing and obtain most of their energy from wind. At the same time, they perturb the atmospheric boundary layer and modulate the momentum transfer across the air-water interface. Such two-way coupling is a distinct feature of wind over the ocean (and other open bodies of water) as opposed to solid boundaries.

There are important applications for modeling the interaction between waves and the boundary layer on top of them. The air-sea momentum flux from this process is an essential boundary condition needed for weather and climate models. The development of offshore wind farms in recent years has also spurred renewed interests in wind-wave coupling, as the wave-modulated boundary layer may have implications for wind turbines that reside at a height comparable to wavelengths of long ocean waves.

Numerical simulations for these applications require modeling approaches of different complexities considering different scales and computational costs. In the context of weather and climate models, Reynolds-averaged Navier-Stokes (RANS) type equations are solved, and the grid is very coarse [$\mathcal{O}$(1-100 km)], which means only averaged effects of waves are modeled, although some regional models have been tested for resolving long waves (Zhu *et al.* 2023). In the context of wind farms and other smaller-scale simulations, large-eddy simulations (LESs) are often employed that can resolve long waves or capture the phase-dependent effects of them (Deskos *et al.* 2021; Aiyer *et al.* 2024; Ayala *et al.* 2024).

Despite their importance, models of wind waves (in the form of wave-averaged parameterizations or subgrid wall models) are limited by a lack of physical understanding of turbulence over moving wavy boundaries, even after continuous theoretical, numerical and observational research over the past few decades. State-of-the-art coupled models

† Courant Institute of Mathematical Sciences, New York University

still parameterize air-sea fluxes using low-order models that consider no or minimal effects of waves (Edson *et al.* 2013). Effects of shorter waves that are not resolved still need to be modeled, which is a non-negligible source of uncertainty in wall-modeled LESs of wind over waves (Husain *et al.* 2019). Incorporating the additional variability due to wave conditions can potentially increase the predictive skills of such models, especially in high-resolution settings and out-of-equilibrium conditions such as storms.

The motivation of our work is to perform high-fidelity direct numerical simulations (DNSs) of wind over waves and to use the physical insights gained as guidance for developing simplified models. In Wu *et al.* (2022) (hereinafter WU22), we conducted fully coupled wind-wave simulations using a geometric volume-of-fluid solver with adaptive mesh refinement (AMR) features and studied wave growth rate under various wind conditions. In this report, we extend the analysis to the rich dynamics in the wave-modulated boundary layer in the form of turbulence statistics.

In addition to analyzing the dynamics of the wave-modulated boundary layer, this work aspires to work toward uncertainty quantification for DNS data sets. There are a few sources of uncertainty in the estimate of turbulence statistics from numerical simulation: turbulence closure models, numerical discretization of the governing equation and finite sampling (Oliver *et al.* 2014). Since we are using DNS, which is a high-fidelity simulation, we assume that the main source of uncertainty is the sampling uncertainty. This is particularly important in our case since the flow is transient in nature due to the full coupling between wind and actively growing waves.

The remainder of this report is structured as follows. In Section 2, the formulation and computational setup are outlined, and an additional forcing scheme for sensitivity test is introduced. Section 3 briefly describes the momentum equation of boundary layer over waves with triple decomposition. Section 4 presents the statistics analyzed based on the DNS data, with a focus on evaluating the sensitivity to forcing schemes and to finite sampling. Finally, conclusions are drawn in Section 5.

## 2. Formulation and computational setup

We solve the (variable density) incompressible Navier-Stokes equations,

$$\frac{\partial \rho}{\partial t} + \nabla \cdot (\rho \mathbf{u}) = 0 \tag{2.1}$$

$$\rho \left( \frac{\partial \mathbf{u}}{\partial t} + (\mathbf{u} \cdot \nabla)\mathbf{u} \right) = -\nabla p + \nabla \cdot (2\mu \mathbf{D}) + \sigma \kappa \delta_S (\mathbf{x} - \mathbf{x}_{\mathcal{F}}) \mathbf{n}, \tag{2.2}$$

$$\nabla \cdot \mathbf{u} = 0, \tag{2.3}$$

where $\mathbf{u}$, $p$ and $\mathbf{D}$ are velocity, pressure and strain rate tensor, respectively. For the surface tension term, $\sigma$, $\kappa$, $\delta_S$, $\mathbf{x}_{\mathcal{F}}$, and $\mathbf{n}$ are surface tension, curvature, Dirac-delta function, interfacial location and the normal vector of the interface, respectively. A volume fraction field $\mathcal{F}(x, y, z, t)$ is introduced, and material properties such as density $\rho$ and viscosity $\mu$ are weighted averaged of that of the two phases, in this case water (subscript $w$) and air (subscript $a$):

$$\rho = \mathcal{F}\rho_w + (1 - \mathcal{F})\rho_a, \quad \mu = \mathcal{F}\mu_w + (1 - \mathcal{F})\mu_a. \tag{2.4}$$

We numerically solve for Eqs. (2.1)–(2.4) with an adaptive octree grid, using the Basilisk numerical solver (Popinet 2009).

To maintain compatibility with the default octree grid, the domain is defined as a cube with size $L_0 = 2\pi$. The setup includes four monochromatic waves in the $x$-direction,
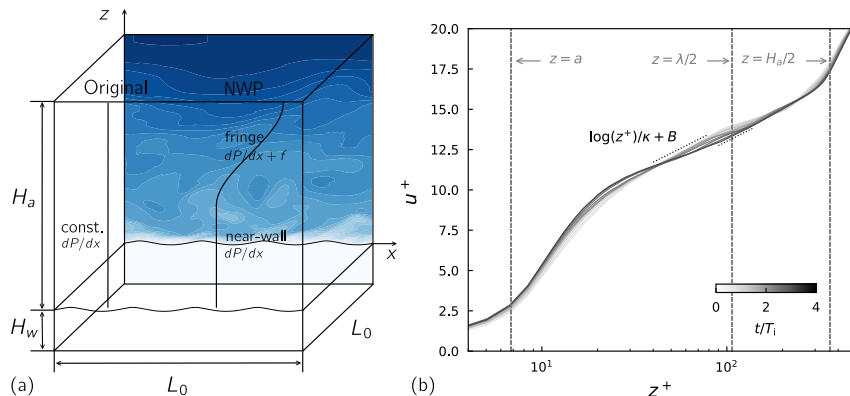
FIGURE 1. (a) Sketch of numerical configuration. (b) Combination of pressure gradient $dP/dx$ and fringe-layer-only acceleration $f$. Grey dashed lines mark a few vertical length scales: $z = a$ shows where the wave crest is; $z = \lambda/2$ shows height corresponding to half wavelength; $z = H_a/2$ shows where the artificial fringe layer in NWP configuration starts.

corresponding to a wavenumber $k = 4$ and wavelength $\lambda = 2\pi/4$. The averaged water depth is $H_w = 1$, resulting in an air side height of $H_a = 2\pi - 1$. The water depth has been verified to be deep enough that the results are not sensitive to $H_w$. Periodic boundary conditions are applied for the horizontal directions. For the top and bottom boundaries, we impose $\partial u/\partial z = \partial v/\partial z = 0$ and $w = 0$.

### 2.1. *Original setup*

In the original setup of WU22, a constant pressure gradient $-(dP/dx)$ is applied uniformly in the air phase to force the boundary layer. The numerical implementation involves adding an acceleration term that is $(1 - \mathcal{F}(x, y, z, t))dP/dx$ at every time step. The dominant stress balance in the horizontal momentum equation leads to

$$-(dP/dx)H_a = \tau_{tot} \equiv \rho_a u_*^2. \tag{2.5}$$

The total wall stress, $\tau_{tot}$, is balanced by vertically integrated pressure gradient and defines the friction velocity $u_*$, which is a parameter that we prescribe *a-priori*. Here, we refer to the stress at the interface as wall stress, since it bears a resemblance to the solid boundary stress in wall-bounded turbulence. We keep in mind, however, that it is a momentum transfer across the two-phase interface. Also note that the stress balance Eq. (2.5) is only exact in an equilibrium (averaged) sense.

### 2.2. *Near-wall-patch configuration*

Inspired by Carney *et al.* (2020), a near-wall-patch configuration is implemented as an additional forcing mechanism to investigate the sensitivity of numerical forcing applied, which should be isolated from the effects of waves on the boundary layer.

The total wall stress is prescribed by selecting the nominal friction velocity $u_*$, such that $\tau_{tot} = \rho_a u_*^2$. A constant background pressure gradient, $dP/dx$, can still be specified throughout the air height $H_a$. In cases where the prescribed wall stress and the pressure gradient $dP/dx$ in Eq. (2.5) are imbalanced, an additional acceleration is applied to a fringe layer within the region $z \in [H_a/2, H_a]$ as

$$f(z) = 4\tau_{turb}(H_a - 2z)^2(5H_a - 4z)/H_a^4, \tag{2.6}$$

where $\tau_{turb} = \tau_{tot} - (dP/dx)H_a$ is the turbulent momentum flux across the fringe layer bottom at $H_a/2$. (We note that the wall normal direction is indicated as $z$ following the convention used in the atmospheric dynamics community and $z = 0$ at the air-water interface.) This formulation guarantees that the partition of $dP/dx$ and $f$ satisfies the vertically integrated streamwise momentum equation,

$$-(dP/dx)H_a + \int_0^{H_a} f(z)dz = \tau_{tot}. \qquad (2.7)$$

The choice of the shape of the auxiliary forcing $f(z)$ is not unique as long as its integrated value satisfies Eq. (2.7). The expression Eq. (2.6) is the one given in Carney *et al.* (2020) and adopted here, which has the property of zero gradient at both $H_a/2$ and $H_a$. In this study, we only consider an extreme case where the pressure gradient $dP/dx$ is zero and the near-wall layer of $z \in [0, H_a/2]$ is forced solely by turbulent momentum flux at $z = H_a/2$. This allows us to construct a zero-pressure-gradient boundary layer.

### 2.3. *Numerical considerations, parameters and notations*

In WU22, a fully developed boundary layer (precursor) is first computed from rest, while keeping the waves stationary by setting the water phase velocity at zero. Then, the waves are released by initializing their orbital velocity. There is an adjustment period upon the sudden introduction of wave motion, and the duration of this stage is found empirically (largely by examining the near-wall stress) to last about $4T_e$, where $T_e = 2\lambda/\langle u \rangle(z = \lambda)$ is the eddy turnover time of an eddy of the size of wavelength $\lambda$ and $\langle u \rangle(z = \lambda)$ is the mean horizontal velocity. We follow this general guideline in the processing of data for this report.

The two forcing setups and an illustration of the computational domain are shown in Figure 1(a). We denote the two forcing setups as "Original" and "NWP-ZPG" (near-wall-patch-zero-pressure-gradient). For generating the precursor for the NWP-ZPG configuration, given that we already have a fully developed precursor in equilibrium with the original forcing, we chose to use it as the initial condition for the NWP-ZPG setup instead of performing a spin-up from rest. Figure 1(b) shows the transitional period after the forcing is switched from Original to NWP-ZPG. This shortcut reveals an interesting behavior of the boundary layer mean velocity profile adapting to the change of forcing. After about $4T_i$ ($T_i$ defined as the inner layer timescale of $0.1H_a/u_*$), the mean profile stabilizes into a new shape where the log layer seems to have shifted toward a larger value of $z^+$. While this is an intriguing problem in its own right, it is beyond the scope of this report to examine the mechanism of the profile shift. In terms of computational cost, there is no significant difference between the NWP-ZPG and the Original setups during runtime.

We investigate slow to intermediate wave speed and denote cases of $c/u_* = [2, 4, 8]$ with [CU2, CU4, CU8]. The wave age $c/u_*$ defines the ratio between the phase speed of waves and characteristic wind speed. We change the gravitational acceleration for different wave ages while keeping the wavelength constant. Therefore, the wavelength and wave phase speed are independent for this idealized study (which is not the case for realistic surface waves). The other nondimensional parameters used are as follows: the density ratio between air and water $\rho_a/\rho_w = 1.225 \times 10^{-3}$; the dynamic viscosity ratio $\mu_a/\mu_w = 1.831 \times 10^{-2} \times [16, 8, 4]$ (corresponding to wave ages $c/u_* = [2,4,8]$); the air-side frictional Reynolds number $Re_\tau = \rho_a u_* H_a/\mu_a = 720$; the initial wave slope $ak$ = 0.2; and the Bond number $Bo = (\rho_w - \rho_a)g/\sigma k^2 = 200$. Quantities normalized by wall units are denoted by a superscription $^+$. Unless otherwise specified, we use the nominal
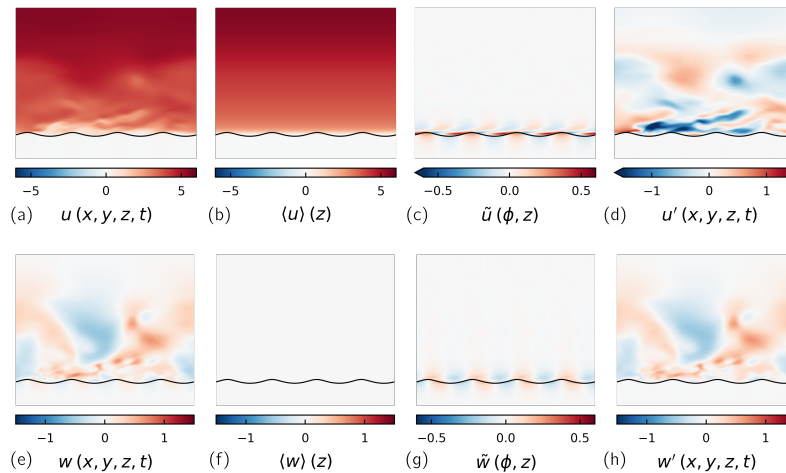
FIGURE 2. Triple decomposition of horizontal and vertical velocity components following Eq. (3.4). Here, they are plotted for the Original CU4 case, but the qualitative picture is similar across all cases. Phase averaging is performed with time sampling windows of around 350 $t_\nu$ (around 6.4 wave periods for CU4).

friction velocity $u*$, length scale $l_\nu = \nu_a/u_*$ and time scale $t_\nu = \nu_a/(u_*)^2$ as wall units. The monochromatic wavelength in wall unit is fixed as $\lambda^+ = \lambda/l_\nu = 214$, while the wave period $T$ in wall unit $T^+ = T/t_\nu \approx [107, 54, 27]$ for $c/u_* = [2, 4, 8]$.

## 3. Momentum equation for boundary layer over waves

Consider a boundary layer flow in the $x$ direction. The velocity vector $\mathbf{u} = (u, v, w)$ can be decomposed into a Reynolds-averaged mean velocity $\overline{\mathbf{u}} = (\bar{u}, \bar{v}, \bar{w})$ and a turbulent fluctuation part $\mathbf{u}' = (u', v', w')$. It is common to consider a boundary layer that is symmetric in the spanwise direction $y$, homogeneous in the streamwise direction $x$ and stationary in $t$. With Reynolds decomposition

$$\mathbf{u}(x, y, z, t) = \overline{\mathbf{u}}(z, t) + \mathbf{u}'(x, y, z, t) \tag{3.1}$$

and the above-mentioned assumptions, the horizontal momentum equation

$$\frac{\partial u}{\partial t} + u\frac{\partial u}{\partial x} + v\frac{\partial u}{\partial y} + w\frac{\partial u}{\partial z} = -\frac{1}{\rho_a}\frac{\partial p}{\partial x} + \nu(\frac{\partial^2 u}{\partial x^2} + \frac{\partial^2 u}{\partial y^2} + \frac{\partial^2 u}{\partial z^2}) \tag{3.2}$$

simplifies to

$$-\frac{1}{\rho_a}\frac{\partial \overline{p}}{\partial x} - \frac{\partial \overline{u'w'}}{\partial z} - \nu\frac{\partial^2 \overline{u}}{\partial z^2} = 0. \tag{3.3}$$

The averaged pressure gradient $\partial\overline{p}/\partial x$ typically comes from varying geometry (e.g., of airfoils) in engineering contexts. For atmospheric boundary layer, it can represent synoptic-scale pressure patterns. In any case, the pressure gradient acts at a horizontal scale larger than the boundary layer thickness and has an accelerating/decelerating effect throughout the total depth of the boundary layer.

For boundary layer flow over waves, the assumption of homogeneity in $x$ no longer

holds. The presence of waves induces periodic perturbations that alter the structure of the turbulent boundary layer. The so-called triple decomposition (Phillips 1966; Hussain & Reynolds 1970) is introduced

$$\mathbf{u}(x, y, z, t) = \langle\mathbf{u}\rangle(z, t) + \tilde{\mathbf{u}}(x, z, t) + \mathbf{u}'(x, y, z, t), \tag{3.4}$$

which has two parts. The first part is the Reynolds decomposition

$$\mathbf{u}(x, y, z, t) = \overline{\mathbf{u}}(\phi = x + c(k)t, z) + \mathbf{u}'(x, y, z, t). \tag{3.5}$$

Here, $\bar{\cdot}$ denotes the Reynolds (ensemble) averaging and is only performed in the statistically homogeneous dimensions (in this case along $y$ and along constant phase lines $\phi$). The second part is the wave decomposition

$$\overline{\mathbf{u}}(\phi, z) = \langle\overline{\mathbf{u}}\rangle(z) + \tilde{\mathbf{u}}(\phi, t) \equiv \langle\mathbf{u}\rangle(z) + \tilde{\mathbf{u}}(\phi, t). \tag{3.6}$$

Here, $\langle\cdot\rangle$ denotes phase averaging, i.e., averaging over wave phase. The bar in $\langle\overline{\mathbf{u}}\rangle(z)$ is dropped for brevity. By definition, $\overline{u'} = 0$ and $\langle\tilde{u}\rangle = 0$. Substituting Eq. (3.5) into the horizontal momentum equation

$$\frac{\partial\overline{u}}{\partial t} + \overline{u}\frac{\partial\overline{u}}{\partial x} + \overline{w}\frac{\partial\overline{u}}{\partial z} + \frac{\partial\overline{u'u'}}{\partial x} + \frac{\partial\overline{u'w'}}{\partial z} = -\frac{1}{\rho_a}\frac{\partial\overline{p}}{\partial x} + \nu\frac{\partial^2\overline{u}}{\partial z^2}, \tag{3.7}$$

we see that there are additional $\partial/\partial x$ terms that cannot be eliminated due to the horizontal inhomogeneity introduced by waves. Furthermore, the pressure term $\overline{p}$ contains not only large-scale gradient but also small-scale variation due to wave perturbation. Triple decomposition [Eq. (3.4)] is required to obtain an equation that does not explicitly depend on wave phase, which reads

$$\frac{\partial\langle\tilde{u}\tilde{w}\rangle}{\partial z} + \frac{\partial\langle u'w'\rangle}{\partial z} = -\frac{1}{\rho_a}\frac{\partial\langle p\rangle}{\partial x} + \nu\frac{\partial^2\langle u\rangle}{\partial z^2}, \tag{3.8}$$

and again $\langle u'w'\rangle$ is shorthand for $\langle\overline{u'w'}\rangle$.

To close the system, one can either model the (phase-dependent) turbulent stress $\overline{u'u'}$ and $\overline{u'w'}$ in the phase-dependent Eq. (3.7) or model the (phase-averaged) wave-induced stress $\langle\tilde{u}\tilde{w}\rangle$ and (phase-averaged) turbulent stress $\langle u'w'\rangle$ in the phase-averaged Eq. (3.8). The other option is to bypass the Reynolds-averaged equation and perform phase-resolved LESs or DNSs. In this work, we conduct two-phase DNS, and as part of the analysis we diagnose the (phase-averaged) wave-induced stress $\langle\tilde{u}\tilde{w}\rangle$ and turbulent stress $\langle u'w'\rangle$ from DNS data. In particular, we compare the stress profile in the Original and NWP setups.

## 4. Results

### 4.1. *Triple decomposition and stress profiles*

Figure 2 shows the triple-decomposed velocity field following Eq. (3.4). The wave-coherent signals $\tilde{u}$ and $\tilde{w}$ are mainly seen in a layer close to the interface and are smaller in magnitude compared to turbulent fluctuation $u'$ and $w'$. The wave-coherent $\tilde{u}$ shows acceleration and deceleration over the windward and leeward parts, respectively; the wave-coherent $\tilde{w}$ shows alternating upward and downward motions.

In Figure 3, we plot the vertical profiles of phase-averaged, wave-induced stress $-\langle\tilde{u}\tilde{w}\rangle$ and turbulent stress $-\langle u'w'\rangle$. Figure 3(a) shows the profiles for the full extent of air-phase height $H_a$. We emphasize that the wave-induced stress only affects a thin layer near the interface, which is a small fraction of $H_a$. In the rest of the domain, turbulent
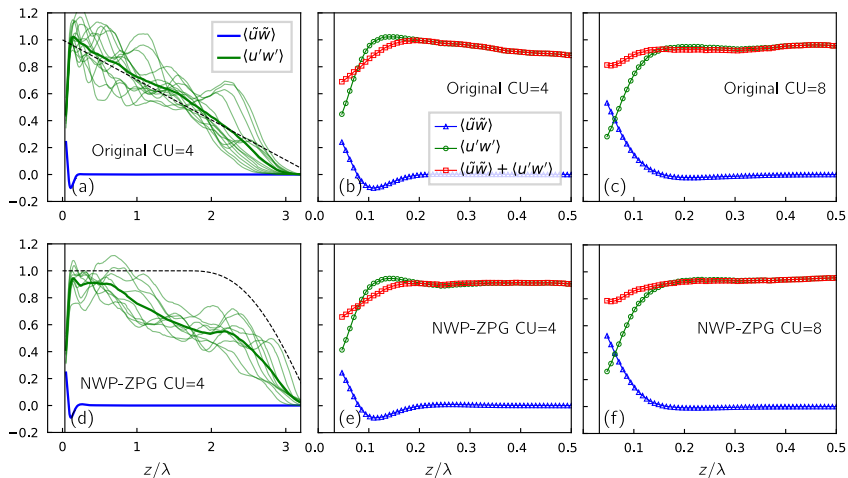
FIGURE 3. (a) Vertical profiles of stress over the full extent of $H_a$, for the Original configuration. (b,c) Vertical profiles of stress zoomed into the near-wave region for the CU4 and CU8 cases. Vertical black line indicates where the wave crest is. The stresses are normalized by the nominal wall stress $\tau_{tot} = u_*^2$. The vertical coordinate is normalized by wavelength $\lambda$. (d-f) The same as (a-c) but for the NWP-ZPG configuration.

stress $\langle u'w' \rangle$ dominates the momentum transport. Each thin green line shows spatially averaged $u'v'$ in one time snapshot, while the thick green line shows additionally time-averaged $\langle u'w' \rangle$. From this we can see that the statistics of $u'w'$ need long sampling time to converge (and they are not fully converged yet in this plot). The wave-coherent signals, by contrast, are largely unaffected by the finite sampling and are confirmed to be statistically converged. Even though not fully converged, the profiles of $\langle u'w' \rangle$ in the Original setup [Figure 3(a)] agree with that of a pressure-driven boundary layer with a flat solid bottom (dashed black line), which decreases linearly with height. For the NWP-ZPG setup [Figure 3(d)], there is a more prominent constant flux layer near the interface that agrees with that of a ZPG boundary layer. Further away from the wall, the turbulent stress deviates from the expected profile of NWP-ZPG (dashed black line). This is likely due to the fact that we transitioned from the original setup precursor to the NWP-ZPG precursor, but the integration time was not long enough for the stress to fully adjust. AMR could also potentially affect the resolved stress profiles, and further examination needs to be done.

Fortunately, the presence of such imbalance in the outer region does not seem to affect the near-wall region, as shown in Figure 3(b), which is a zoomed-in view of the stress profiles. For both CU4 and CU8, the change of total stress in $[0, 0.5\lambda]$ is small and can be approximated as a constant even for the Original pressure-driven case. The profiles of $\langle \tilde{u}\tilde{w} \rangle$ in Original and NWP-ZPG are nearly identical. This indicates that the near-wave dynamics are unaffected by the large-scale forcing scheme.

By comparing the two cases with different wave ages, CU4 and CU8, we can see the effect of wave condition on wave-induced stress $\langle \tilde{u}\tilde{w} \rangle$. The vertical extent of the nonzero region is similar, but the shape is different. In agreement with physical intuition, the length of the wave-affected layer scales with wavelength but only weakly depends on wave age. A more complete parameter space needs to be explored before drawing definite
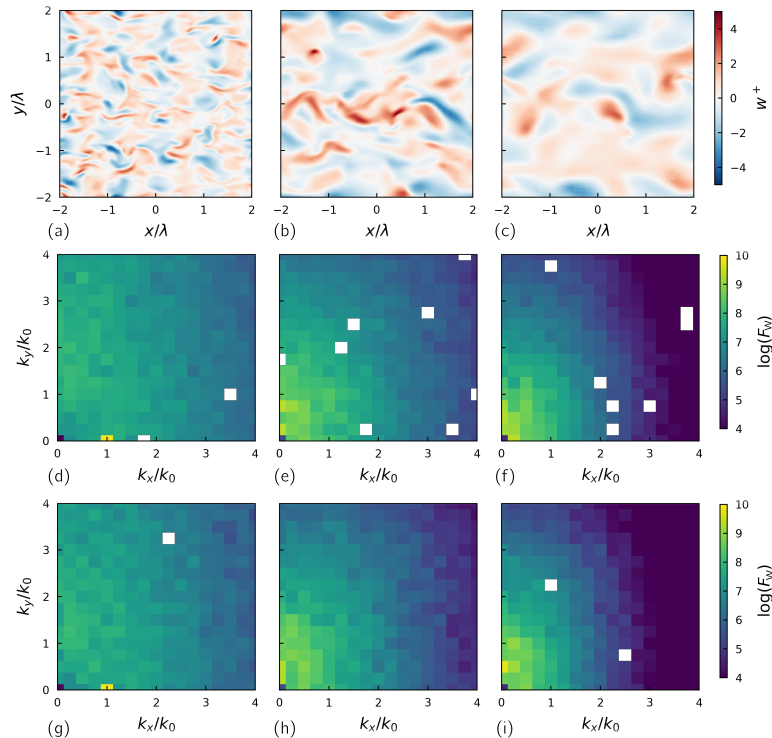
FIGURE 4. (a-c) Instantaneous vertical velocity $w$ at three different heights $z/\lambda = 0.1, 0.5, 1$ ($z^+ = 21, 107, 214$). Wavenumbers are normalized by the imposed surface wave $k_0 = 2\pi/\lambda$. (d-f) Horizontal wavenumber spectrum for CU4 in the Original setup at three different heights. (g-i) The same spectrum as in (d-f) but for the NWP-ZPG setup.

conclusions. Also note that we use absolute coordinate $x - y - z$ in our processing of the data, which means only the region above the wave crest (shown by the black line) is physically meaningful. To obtain well-defined, wave-induced stress all the way down to the wave surface, one needs to resort to wave-fitted curvilinear coordinates, which has been adopted by the majority of literature [e.g., in DNS of Yang & Shen (2010), LES of Husain *et al.* (2019) and laboratory experiments of Yousefi *et al.* (2020)]. Statistics in absolute coordinates suffice for the purpose of qualitative analyses of these profiles, and our results are in general agreement with the above-mentioned works. However, any discrepancy of the wave-induced stress might be due to the coordinate choice, as pointed out by Yousefi *et al.* (2020).

### 4.2. *Wavenumber spectrum*

Figure 4(a) shows vertical velocity at three cross sections $z/\lambda = 0.1, 0.5, 1$ (in wall unit $z/\lambda = 21, 107, 214$). The near-wall region shows clear modulation from waves, which is also indicated by the peak spectral signal at wavenumber $k_x = k_0$ in Figure 4(b). Further away from the waves, the modulation is less prominent, and large-scale structures instead play a dominant role. Figure 4(b,c) compare the spectrum obtained in Original and NWP-ZPG setups. At $z/\lambda = 0.1$, the spectra are very similar, which again confirms that the near-wave dynamics are dominated by perturbation from surface waves and less affected
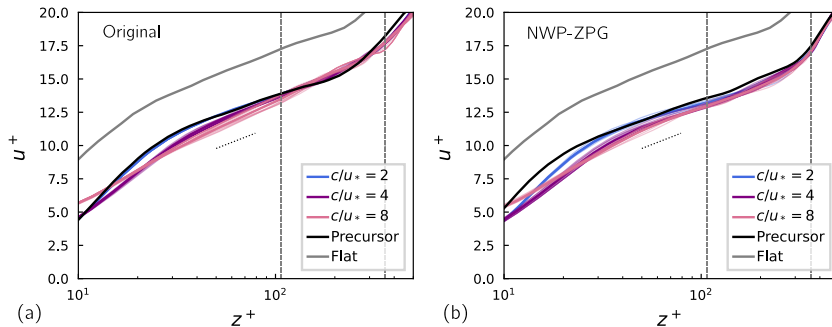
FIGURE 5. Mean velocity profile in wall units for CU2, CU4 and CU8 in the Original setup (a) and NWP-ZPG setup (b). Black dotted line shows the $1/\kappa \log(z^+)$ slope in $z^+ \in [50, 80]$, which is the range we used to fit the roughness parameter.

| $c/u_*$ | 2 | 4 | 8 |
|---|---|---|---|
| Original | [0.331, 0.334] | [0.395, 0.407] | [0.473, 0.514] |
| NWP-ZPG | [0.391, 0.402] | [0.461, 0.488] | [0.484, 0.508] |

TABLE 1. Range of roughness length $z_0^+$ values extracted from the mean profiles.

by large-scale forcing. At $z/\lambda = 0.5$ and 1, the NWP-ZPG case has less energy in large scales but more concentrated energy in small scales.

To quantify the sampling uncertainty in our spectrum computation, we compute the standard deviation using different time snapshots divided by the square root of total sample numbers $\sigma(k_x, k_y) = \sum_1^{N_t} (F_w(k_x, k_y, t) - F_w(k_x, k_y))^2/\sqrt{N_t}$. In Figure 4 (b,c) we have masked out the pixels with a fractional standard deviation $\sigma(k_x, k_y)/F_w(k_x, k_y)$ of more than 20%. The rest of the spectral components are of statistical significance deemed by this ad-hoc standard.

### 4.3. *Estimate of roughness length from mean profiles*

The last part of this analysis is devoted to discussing the mean profiles and the derived roughness length, which is a popular modeling parameter in wall-resolved LES and RANS.

We sample the spatially averaged mean velocity every 0.1 computational time units (around 3.4 $t_\nu$). Thick curves in Figure 5 are averaged over 100 samples, while the thin opaque curves are averaged over 10 samples, which exhibit some level of variability in the mean profiles. There seems to be more variability in the higher wave age cases, which we do not yet understand.

For reference, the mean profiles of the precursor (when the waves are not moving) and of a flat surface case of the same $Re_\tau$ (taken from WU22) are shown. There is a significant downshift from the flat wall case in the current group of cases with $ak = 0.2$, but much less difference between varying wave age cases. This minor effect of wave age on mean profiles aligns with our previous observations and suggests that the main factor influencing roughness (i.e., drag) is the steepness of waves and other geometric properties of the wave crests rather than wave age.

In Table 1, we list the roughness length (in wall unit) $z^+$ in the Original and the

NWP-ZPG setups. A sliding window of 50 samples was used, and instead of one value, the interval of maximal and minimal values of fitted $z_0$ from such windows is reported to account for the variability mentioned earlier. The roughness length is larger in the NWP-ZPG cases than in the Original cases for all three wave ages. By contrast, the difference of $z^+$ between different wave ages is smaller in the NWP-ZPG setup. This shows the sensitivity of the main profiles (and consequently fitted roughness length value) to the forcing scheme, which is perhaps exacerbated by the relatively small Reynolds number in our simulations.

Despite the sensitivity of the roughness length parameter to processing and simulation setup, we can still gain some insights from its trend and range of values. Consistent in both setups, we see that for the same wave steepness there is a rather small increase in $z_0^+$ as the wave age increases, which is counterintuitive. The range of $z_0^+$ from 0.3 to 0.5 is larger than the smooth flat wall value (around 0.11), but can still be categorized as being in the hydraulically smooth regime that is usually defined as $z_0^+$ smaller than 5 (Flack & Schultz 2010). This is an important point: the resolved smooth monochromatic waves themselves, without small-scale ripples or crest steepening due to nonlinear effects, are not rough and interact with the boundary layer in a very different way from roughness elements in engineering flows. Admittedly, the scenario might be different for a higher Reynolds number and a much thinner viscous sublayer.

### 4.4. *Discussion on the applicability of DNS data in subgrid modeling*

The challenge remains as to effectively use DNS data to enhance simpler models of momentum flux (e.g., wall models) in wave-averaged or long-wave-resolved simulations. One feasible approach is to treat DNS as a small computational unit for modeling ripples on the order of $\mathcal{O}(1\text{-}10 \text{ cm})$, which can help in developing closure models for wall-modeled LES. To account for the influence of larger scales that exceed the DNS domain, background forcing should be introduced to represent these modulations. One example is to use a modified gravity to represent the location of ripples (resolved in DNS) on the crest or trough of long waves (not resolved in DNS). An alternative to the traditional equilibrium wall model with a roughness parameter, which assumes that the first grid point in LES resides in the log layer, may be worth exploring. This could provide a more accurate representation of the near-wall dynamics in complex wave environments. Another approach is to directly compare DNS with wave-resolved LES, despite differences in Reynolds numbers. In this case, the comparison should focus on the flow structure, such as turbulent and wave-induced stress in the near-wave region, rather than on the mean profiles alone. Direct comparisons of mean profiles could be misleading due to the absence of background ripples in the DNS, which leads to reduced drag compared to wall-modeled LES.

## 5. Conclusions

The two-phase, fully-coupled DNS of wind-wave interaction from WU22 is further developed, and an additional forcing scheme based on the idea of a near-wall-patch forcing method is investigated for three different wave ages. Statistics from this DNS data set, including the vertical turbulent and wave-induced stress profiles, the horizontal spectra at different cross sections, and the mean velocity profiles, are presented.

From the flow field triple decomposition and the wavenumber spectra, we conclude that changing the setup from a pressure-driven boundary layer to a zero-pressure-gradient boundary layer near the waves does not significantly affect the near-wave dynamics,

which confirms the dominant role of wave perturbation in the near-wall region. The vertical stress profiles indicate that the length of the wave-affected layers scales with wavelength but is less affected by the wave age. The mean velocity profiles show some level of sensitivity to large-scale forcing. In particular, the roughness length in the NWP-ZPG setup showed slightly larger values than that of the Original setup. Further studies and a statistically converged precursor are needed to further confirm that and to understand how the near-wave region interacts with large-scale motion away from the interface.

## REFERENCES

AIYER, A. K., DEIKE, L. & MUELLER, M. E. 2024 A dynamic wall modeling approach for large eddy simulation of offshore wind farms in realistic oceanic conditions. *J. Renew. Sustain. Ener.* **16** (1), 013305.

AYALA, M., SADEK, Z., FERČÁK, O., CAL, R. B., GAYME, D. F. & MENEVEAU, C. 2024 A moving surface drag model for LES of wind over waves. *Bound.-Lay. Meteorol.* **190**, 39.

CARNEY, S. P., ENGQUIST, B. & MOSER, R. D. 2020 Near-wall patch representation of wall-bounded turbulence. *J. Fluid. Mech.* **903**, A23.

DESKOS, G., LEE, J. C. Y., DRAXL, C. & SPRAGUE, M. A. 2021 Review of wind-wave coupling models for large-eddy simulation of the marine atmospheric boundary layer. *J. Atmos. Sci.* **78**, 3025–3045.

EDSON, J. B., JAMPANA, V., WELLER, R. A., BIGORRE, S. P., PLUEDDEMANN, A. J., FAIRALL, C. W., MILLER, S. D., MAHRT, L., VICKERS, D. & HERSBACH, H. 2013 On the exchange of momentum over the open ocean. *J. Phys. Oceanogr.* **43**, 1589–1610.

FLACK, K. A. & SCHULTZ, M. P. 2010 Review of hydraulic roughness scales in the fully rough regime. *J. Fluids Eng.* **132** (041203).

HUSAIN, N. T., HARA, T., BUCKLEY, M. P., YOUSEFI, K., VERON, F. & SULLIVAN, P. P. 2019 Boundary layer turbulence over surface waves in a strongly forced condition: Les and observation. *J. Phys. Oceanogr.* **49**, 1997–2015.

HUSSAIN, A. K. M. F. & REYNOLDS, W. C. 1970 The mechanics of an organized wave in turbulent shear flow. *J. Fluid. Mech.* **41**, 241–258.

OLIVER, T. A., MALAYA, N., ULERICH, R. & MOSER, R. D. 2014 Estimating uncertainties in statistics computed from direct numerical simulation. *Physics of Fluids* **26**, 035101.

PHILLIPS, O. M. 1966 *The Dynamics of the Upper Ocean*. Cambridge University Press.

POPINET, S. 2009 An accurate adaptive solver for surface-tension-driven interfacial flows. *J. Comput. Phys.* **228**, 5838–5866.

WU, J., POPINET, S. & DEIKE, L. 2022 Revisiting wind wave growth with fully coupled direct numerical simulations. *J. Fluid. Mech.* **951**, A18.

YANG, D. & SHEN, L. 2010 Direct-simulation-based study of turbulent flow over various waving boundaries. *J. Fluid. Mech.* **650**, 131–180.

YOUSEFI, K., VERON, F. & BUCKLEY, M. P. 2020 Momentum flux measurements in the airflow over wind-generated surface waves. *Journal of Fluid Mechanics* **895**, A15.

ZHU, P., LI, T., MIROCHA, J. D., ARTHUR, R. S., WU, Z. & FRINGER, O. B. 2023 A moving-wave implementation in wrf to study the impact of surface water waves on the atmospheric boundary layer. *Mon. Weather Rev.* **151**, 2883–2903.